

Unraveling the Voltage-Fade Mechanism in High-Energy-Density Lithium-Ion Batteries: Origin of the Tetrahedral Cations for Spinel Conversion

Debasish Mohanty,^{*,†} Jianlin Li,[†] Daniel P. Abraham,[‡] Ashfia Huq,[§] E. Andrew Payzant,[§] David L. Wood, III,^{*,†,||} and Claus Daniel^{*,†,||}

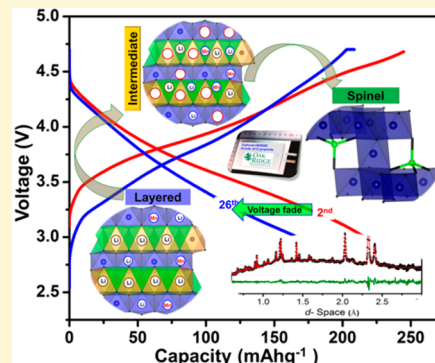
[†]Energy and Transportation Science Division and [§]Chemical and Engineering Materials Division, Oak Ridge National Laboratory, Oak Ridge, Tennessee 37831, United States

[‡]Chemical Sciences and Engineering Division, Argonne National Laboratory, Argonne, Illinois 60439, United States

^{||}Bredesen Center for Interdisciplinary Research and Graduate Education, University of Tennessee, Knoxville, Tennessee 37996, United States

Supporting Information

ABSTRACT: High-voltage layered lithium- and manganese-rich (LMR) oxides have the potential to dramatically enhance the energy density of current Li-ion energy storage systems. However, these materials are currently not used commonly; one reason is their inability to maintain a consistent voltage profile (voltage fade) during electrochemical cycling. This report rationalizes the cause of this voltage fade by providing evidence of layered to spinel (LS) structural evolution pathways in the host $\text{Li}_{1.2}\text{Mn}_{0.55}\text{Ni}_{0.15}\text{Co}_{0.1}\text{O}_2$ oxide. By employing neutron powder diffraction, we show that LS structural rearrangement in the LMR oxide occurs through a tetrahedral cation intermediate via the following: (i) diffusion of lithium atoms from octahedral to tetrahedral sites of the lithium layer [$(\text{Li}_{\text{Li},\text{oct}} \rightarrow \text{Li}_{\text{Li},\text{tet}})$] which is followed by the dispersal of the lithium ions from the adjacent octahedral site of the metal layer to the tetrahedral sites of lithium layer [$(\text{Li}_{\text{TM},\text{oct}} \rightarrow \text{Li}_{\text{Li},\text{tet}})$]; (ii) migration of Mn from the octahedral sites of the transition-metal layer to the “permanent” octahedral site of lithium layer via tetrahedral site of lithium layer [$(\text{Mn}_{\text{TM},\text{oct}} \rightarrow \text{Mn}_{\text{Li},\text{tet}} \rightarrow \text{Mn}_{\text{Li},\text{oct}})$]. These findings open the door to potential routes to mitigate this “atomic restructuring” in the high-voltage LMR composite oxide by manipulating their composition/structure for practical use in high-energy-density lithium-ion batteries.



INTRODUCTION

As energy and power requirements in all-electric vehicles (EVs) become more demanding, lithium ion batteries (LIBs) are expected to provide the necessary high-energy densities.¹ Lithium- and manganese-rich nickel–manganese–cobalt (LMR-NMC) layered composite oxides with a chemical formula $\text{Li}_{1+x}\text{M}_{1-x}\text{O}_2$ ($\text{M} = \text{Ni, Mn, Co}$) are one of the most promising cathode candidates for high-energy-density LIBs.² When compared with stoichiometric NMC-type oxides (example: $\text{LiMn}_{1/3}\text{Ni}_{1/3}\text{Co}_{1/3}\text{O}_2$), LMR-NMC oxides show higher charge/discharge capacity, typically $\geq 240 \text{ mA h g}^{-1}$ when cycled to a high *upper cutoff voltage* ($\geq 4.5 \text{ V}$) and low *lower cutoff voltage* ($\leq 2.5 \text{ V}$).³ Despite delivering this high capacity, LMR-NMC oxides suffer from voltage fade during electrochemical cycling which precludes their use in practical energy storage devices.^{4,5} The main issue with voltage fading is that it continuously alters the cell capacity associated with a given state of charge (SOC) and, hence, cannot satisfy constant power and energy requirements during operation.³ Depression of the voltage profile decreases the specific energy density of

LIBs (specific energy density = specific capacity \times average operating voltage) which eventually leads to device failure.

Extensive efforts are being made, especially at U.S. national laboratories, to understand and mitigate the voltage fade in LMR-NMC oxides.⁶ In situ X-ray diffraction,⁷ selected area electron diffraction,⁸ high-resolution transmission electron microscopy,^{8,9} and scanning transmission electron microscopy¹⁰ collectively indicate that a “layered to spinel” (LS) structural modification/rearrangement is one of the major reasons for voltage fade in the LMR-NMC composite oxides.¹¹ In addition, surface coatings applied to these oxide particles has shown little or no effect in eliminating the voltage-fade phenomenon, confirming that voltage fade is a bulk, intrinsic property of the oxide.^{6,12} However, the mechanism of this structural rearrangement is not fully understood. The mechanism of this intriguing process needs to be confirmed so that the oxide’s composition/structure can be manipulated

Received: August 26, 2014

Revised: September 23, 2014

Published: September 30, 2014

to suppress this voltage-fade process. The mechanism of structural rearrangement can be understood by answering the following important questions: (1) Which transition-metal ions migrate or relocate in the structure to form the spinel framework? (2) What sites do the relocated transition-metal and lithium ions occupy? (3) What type of spinel phase is formed and how is it formed? (4) What is the migration path for LS structural rearrangements?

The present investigation addresses these important questions by acquiring structural information from cycled LMR-NMC oxides at designated voltages to track the pathways for the LS structure evolution process. We chose the TODA HE5050 LMR-NMC oxide with composition $\text{Li}_{1.2}\text{Mn}_{0.55}\text{Ni}_{0.15}\text{Co}_{0.1}\text{O}_2$ (or $0.5\text{LiNi}_{0.375}\text{Mn}_{0.375}\text{Co}_{0.25}\text{O}_2$; $0.5\text{Li}_2\text{MnO}_3$ in a two-component notation) because this particular material has shown to be an effective high-voltage cathode when cycled to high cutoff voltages and exhibits significant voltage fading in a relatively small number of cycles.^{7,13}

This study utilizes advanced bulk materials characterization technique such as neutron powder diffraction (ND) to investigate the cation migration pathways for LS structural rearrangement. We show that the LS transformation in the LMR-NMC oxide takes place via intralayer Li migration from octahedral to tetrahedral sites and interlayer Mn migration from octahedral sites in the transition-metal layer to octahedral sites in the lithium layer via lithium-layer tetrahedral sites. The approach takes advantage of the uniqueness of the ND technique for locating lighter atoms in the presence of heavier atoms and, therefore, makes it possible to get more accurate structural information about lithium in a transition-metal ion (TM) environment.¹⁴

The information in this article is discussed in three major segments. First, evidence is shown of LS structural transformation in the HE5050 composite oxide causing voltage fade in a *full LIB pouch cell* (section 3.1). Second, cation migration pathways and the mechanism for this transformation (section 3.2) are shown. Lastly, based on this mechanism, potential routes are suggested to overcome the LS transformation that could ultimately suppress the voltage-fade phenomenon (section 3.3).

2. EXPERIMENTAL SECTION

2.1. Materials, Slurry Preparation, and Electrode Coating.

The HE5050 oxide powder used in this study was synthesized by TODA America, Inc., and the composition, ex and in situ X-ray diffraction (XRD), particle morphology, selected area electron diffraction (SAED), high-resolution transmission electron microscopy image, and electrochemical performance data can be found in earlier reports.^{7,13} The electrodes for this study were fabricated at the U.S. Department of Energy Battery Manufacturing R&D facility (BMF)¹⁵ at Oak Ridge National Laboratory (ORNL). Polyvinylidene fluoride (PVDF) (Solvay 5130) and Super P Li (Timcal) in 86/8/6 wt % were dispersed in N-methyl-2-pyrrolidone with a planetary mixer (Ross PDM-1/2). The HE5050 cathode was coated on one side of a 15 μm thick Al foil by a slot-die coater (Frontier Industrial Technology, Inc.). The wet coating thickness was 118.5 μm , and the areal weight was 9.8 cm^2 . For the anode, A12 natural graphite (ConocoPhillips) was used.³

2.2. Pouch Cell Fabrication and Electrochemical Cycling.

Uncalendared HE5050 cathodes and graphite anodes were punched into layers. The areas of a single layer of cathode and anode were 47 and 50 cm^2 , respectively. Three layers of HE5050 cathodes and graphite anodes were assembled into pouch cells (inset of Figure 2) at the ORNL BMF. The reason for making a 3 \times 3 layer pouch cell was to obtain enough material for ND experiments at the POWGEN

beamline¹⁶ at the ORNL Spallation Neutron Source (SNS), which generally requires a sample size of ~ 1 g for this family of materials to obtain refinable patterns. Celgard 2325 was used as the separator; the electrolyte was 1.2 M LiPF₆ in ethylene carbonate:diethyl carbonate (3/7 wt % ratio, Novolyte). All cells underwent formation cycling following a procedure similar to that reported by Abraham's group¹⁷ carried out in two steps. The cells were first cycled three times between 2.2 and 4.1 V to enable complete wetting of the electrochemically active surfaces. Subsequently, the cells underwent two cycles between 2.2 and 4.6 V to "activate" the oxide material; $\sim \text{C}/15$ rate was used in both steps. Next, the cells were cycled between 2.5 and 4.7 V for 26 cycles at a rate of 20 mA/g. Oxide electrode samples for neutron diffraction studies were collected at different cell voltages during the 2nd and 26th charge-discharge cycles after the formation cycling. All pouch cells were disassembled in an argon atmosphere glovebox, washed with dimethyl carbonate, and dried for several hours in the glovebox. Cycled HE5050 oxide powder materials (along with the PVDF and carbon black) were removed from the Al current collectors after being dried. To track the structural rearrangement in the HE5050 material, cycled samples were collected at the voltages shown in parts (a) and (b) of Figure 1 for the 2nd and 26th cycles,

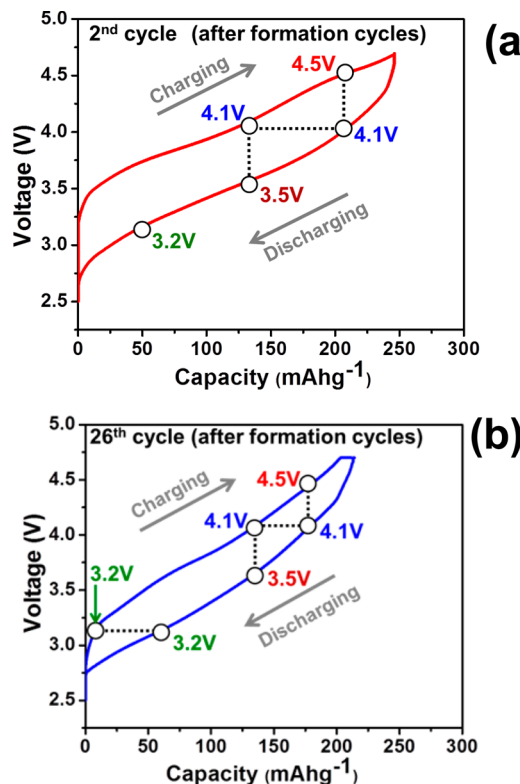


Figure 1. Voltage–capacity curve during the 2nd (a) and 26th cycle (b). The HE5050 oxides were collected at the designated cell voltages for characterization. The connected lines represent the samples collected at the same voltage or same capacity.

respectively. Cell voltages of 3.2, 3.5, 4.1, and 4.5 V were selected as points of interest for structural characterization. The cells underwent a holding/resting period to attain structural equilibrium, and sufficient caution was taken to attain the desired voltages before the cells were disassembled. That is, the reported voltages represent completely relaxed and stabilized HE5050 oxide samples.

2.3. Characterization. **2.3.1. Neutron Diffraction.** HE5050 powder materials were filled in airtight 6 mm vanadium sample cans in an argon-filled glovebox. The cans were transported to the ORNL SNS, where room-temperature ND experiments were carried out on the POWGEN beamline. The 24-sample changer was used to collect the room-temperature ND patterns using a beam of neutrons with a

center wavelength of 1.066 Å. The experimental patterns were refined by the Rietveld method using GSAS¹⁷ and the EXPGUI¹⁸ interface. The neutron diffraction pattern in the lower *d*-spacing range shows “background” (for example, see Figure 6) which is due to the presence of hydrogen (from the binder) in the harvested cycled materials.

2.3.2. X-ray Diffraction. A PANalytical X’Pert Pro system with a molybdenum source ($\lambda = 0.76$ Å) and automatic divergence and antiscatter slits operated at 60 kV and 45 mA was used to collect XRD patterns from pristine and cycled electrodes.

3. RESULTS AND DISCUSSION

3.1. Evidence of LS Transformation Causing Voltage Fade. The electrochemical experiments from LIB pouch cells containing the HE5050 LMR-NMC cathode and graphite anode showed a ~15% loss of specific discharge capacity (Figure 2b) after electrochemical cycling (26 cycles). More

LiMO₂ phase ($R\bar{3}m$ space group) and Li₂MnO₃-like phase ($C2/m$ space group) and has been reported previously.⁷ Presence of the Li₂MnO₃ component was confirmed by the less-intense (extra) XRD peaks at lower 2θ angles, suggesting the presence of lithium in the transition-metal layers (LiMn₆-like regions or cation ordering). It is difficult to distinguish a single monoclinic phase with planar defects from a composite of Li₂MnO₃ and LiMO₂ in TEM and diffraction experiments. However, in our previous study, the composite structure of pristine HE5050 oxide was verified by temperature-dependent magnetic susceptibility experiment and the neutron powder diffraction pattern (ND).^{14a} The Rietveld refinement of ND data showed that pristine HE5050 oxide may be described as 0.50{Li_{1-x}Ni_x}·{Li_{2.0+x}Co_{0.25}Mn_{0.375}Ni_{0.375-x}}O₂·0.50Li₂MnO₃, where $x = 0.0354$, or Li_{1.2}Mn_{0.55}Ni_{0.15}Co_{0.1}O₂ with small (~3%) Li/Ni exchange between octahedral lithium (3b) and octahedral TM (3a) sites in the trigonal phase.^{14a}

The structure of HE5050 oxide alters during the 2nd cycle and significant structural evolution was observed on extended cycling (up to 26 cycles). We first examined the cycled HE5050 oxide by XRD (Figures S1 and S2 in the Supporting Information), and our key findings are as follows: (1) The intensity of cation ordering peaks (020)_M and (110)_M (*M*: monoclinic) decreases after the 2nd cycle (3.2 V discharged state) and are not observed for HE5050 oxides during the 26th cycle (note that these 2nd and 26th cycles are after formation cycles) regardless of cell voltage (Figures S1a–f and S2a–g), which indicates that the Li₂MnO₃ component is reduced on extended cycling (26 cycles). (2) Significant lattice expansion is observed after 26 cycles (3.2 V discharged state), which is seen from the shifting of (003)_R (*R* = rhombohedral) to higher *d*-spacings (lower 2θ angle) (Figure S3). This shift indicates the presence of vacancies in the lithium layer increases the electrostatic repulsion between adjacent cubic-closed-packed (CCP) oxygen layers. (3) Significant peak broadening and changes in peak intensity ratio of (003) and (104) during the 26th cycle (Figure S2) indicates structural changes in the oxide.

The structural/phase evolution was further confirmed by the ND patterns collected at different cell voltages during the 2nd and 26th cycle (Figures S4 and S5). Some structural rearrangement is seen after the 2nd cycle (see section 3.2) but bigger changes are evident after the 26th cycle. We examined each lattice peak in the ND patterns from the cycled HE5050 oxides. Evidence of the presence of a spinel structure can be confirmed from the fact that the (110)_R and (108)_R reflections changed their *d*-spacings during the 2nd charge–discharge cycle; however, the original pristine material structure is retained (Figure 3a). Interestingly, during the 26th cycle (Figure 3b), the lattice spacing difference between (110) and (108) increases as compared to the difference in spacings in the pristine HE5050 material and in the oxide discharged to 3.2 V during the 2nd cycle. The intensity of the (108) peak decreased and moved significantly toward higher *d*-spacing, which provides evidence of a spinel-like phase¹⁹ in the 26th cycle pattern. Further examination (Figure 3c) indicates the presence of a new peak at $d \sim 1.13$ Å, possibly (440) reflection from a unit cell with $Fd\bar{3}m$ space group. The (440) peak from a spinel unit cell has a distinct *d*-spacing as compared to those of trigonal and monoclinic unit cells. In addition, a shoulder before the (201)_R or (400)_M in the cycled oxide obtained in the 26th cycle at 3.2 V discharged state (not in the pristine and oxides in the 2nd cycle at 3.2 V discharged state) further indicates the presence of a spinel structure. Moreover, Rietveld

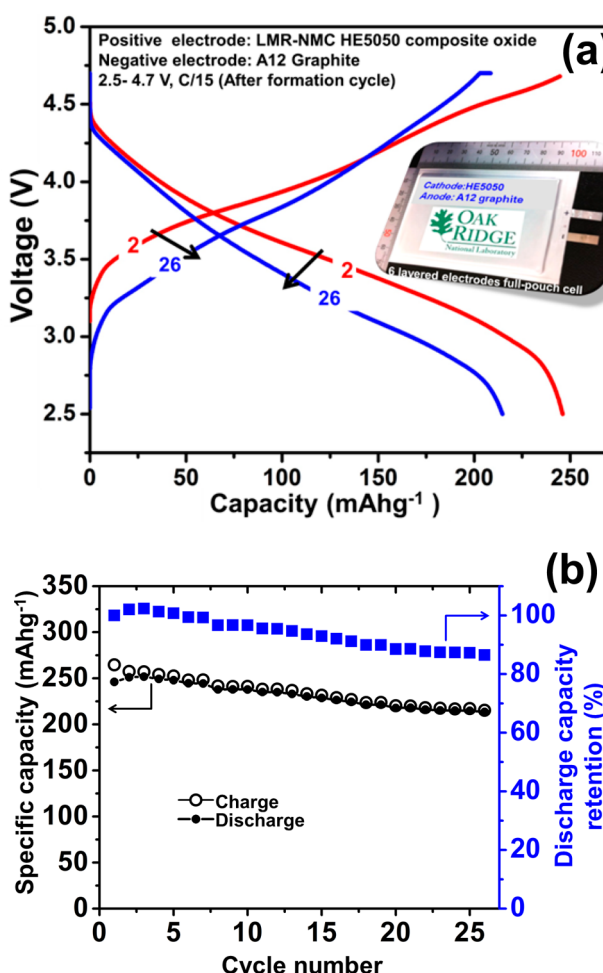


Figure 2. Voltage profile (a) and performance data (b) of a full-pouch cell containing three HE5050 cathodes and three graphite anodes (see inset of Figure 2a). The arrows in Figure 2a show the voltage fade phenomena. The discharge capacity retention shows 15% reduction of discharge capacity after 26 cycles.

importantly, a downward shift of the average voltage (Figure 2a) was observed, which indicates that the voltage-fade phenomenon had occurred (see the arrow marks in Figure 2a) after 26 cycles. In this section, we will show that voltage fade is the effect of structure evolution in the cycled HE5050 oxide. The pristine HE5050 oxide structure is a composite between O₃ oxygen stacked layered rhombohedral or trigonal

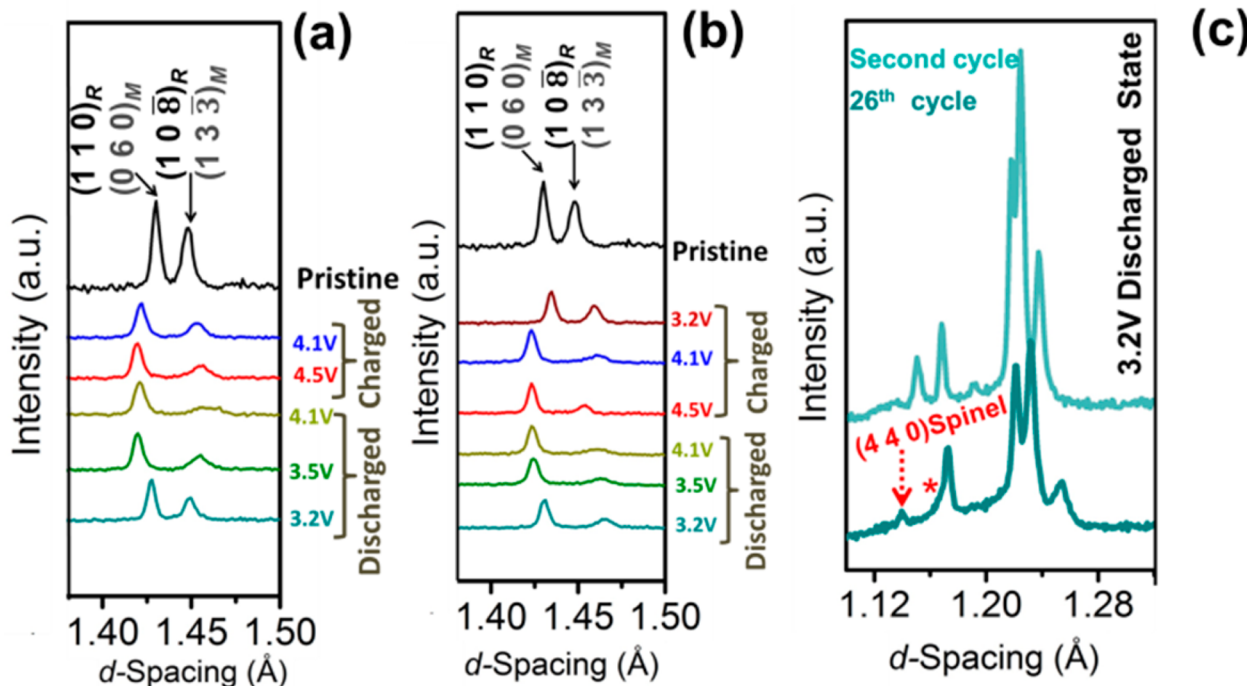


Figure 3. (108) and (110) peak positions in the 2nd (a) and 26th (b) cycle. New peaks at $d = 1.13 \text{ \AA}$ appear at the 3.2 V discharged state after the 26th cycle but not observed after the 2nd cycle (c).

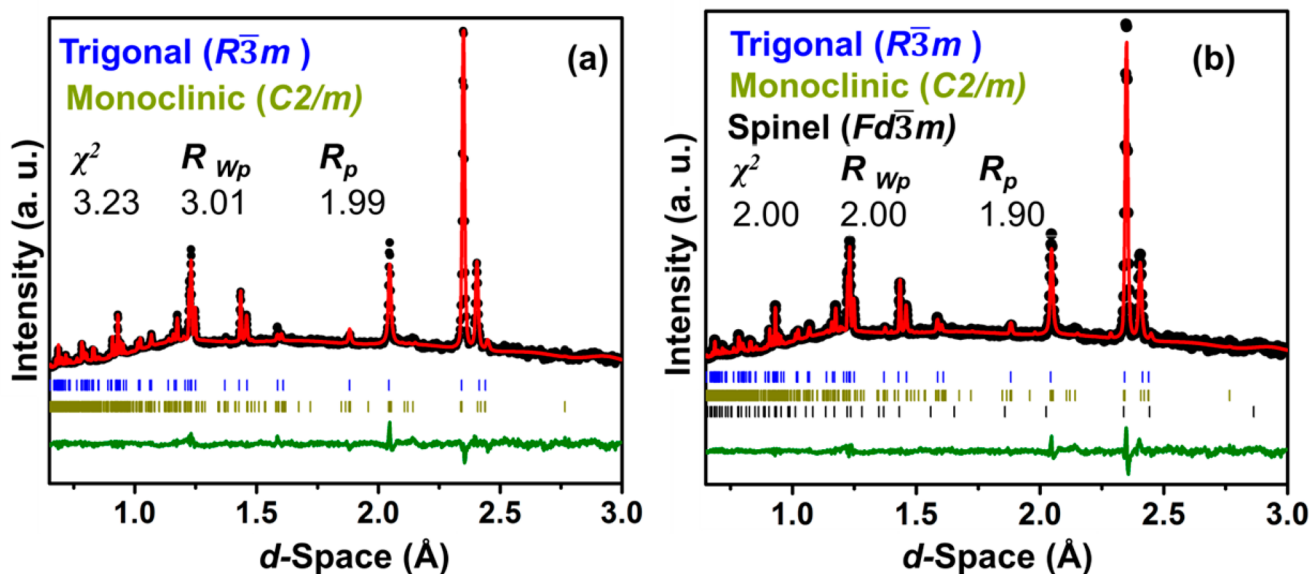


Figure 4. Refined ND patterns for HES050 oxide collected after the 26th cycle at 3.2 V discharged state without spinel phase (a) and with the spinel phase (b) in the model. The model includes spinel phase showing better agreement parameter as compared to the model without the spinel phase.

refinements of the cycled HES050 oxides in the 26th cycle showed improved agreement by the addition of a spinel component (LiMn_2O_4 model). In contrast, no improvements in the fitting were observed for oxides from the 2nd cycle. The refinement indicated $\sim 15\%$ by weight of a spinel component in the oxide structure after the 26th charge–discharge cycle. Figure 4 shows fitting patterns and agreement parameters from the Rietveld refinements of oxides discharged to 3.2 V for the 26th cycle in which a LiMn_2O_4 spinel phase was not included (Figure 4a) and included (Figure 4b).

To summarize, (1) structural modification might occur during the initial cycles, but that it might be minimal and

reversible. This is evidenced by ND peak analysis, where the peaks from HES050 oxides after the 2nd cycle (3.2 V discharged state) attain the initial positions very close to the starting material. (2) XRD showed peak broadening, change in intensity ratio of (003) and (104) peaks, and suppression of the layered character after extended cycling. (3) ND showed a new spinel-like (440) peak at $d = 1.13 \text{ \AA}$, and an increase in lattice spacing of (110) and (108) reflections after extended cycling.

These results above indicate that HES050 oxide undergoes a LS structural transformation after extended cycling (26 cycles in this study), which is in agreement with the high-resolution TEM and SAED data reported previously.¹³ The formation of a

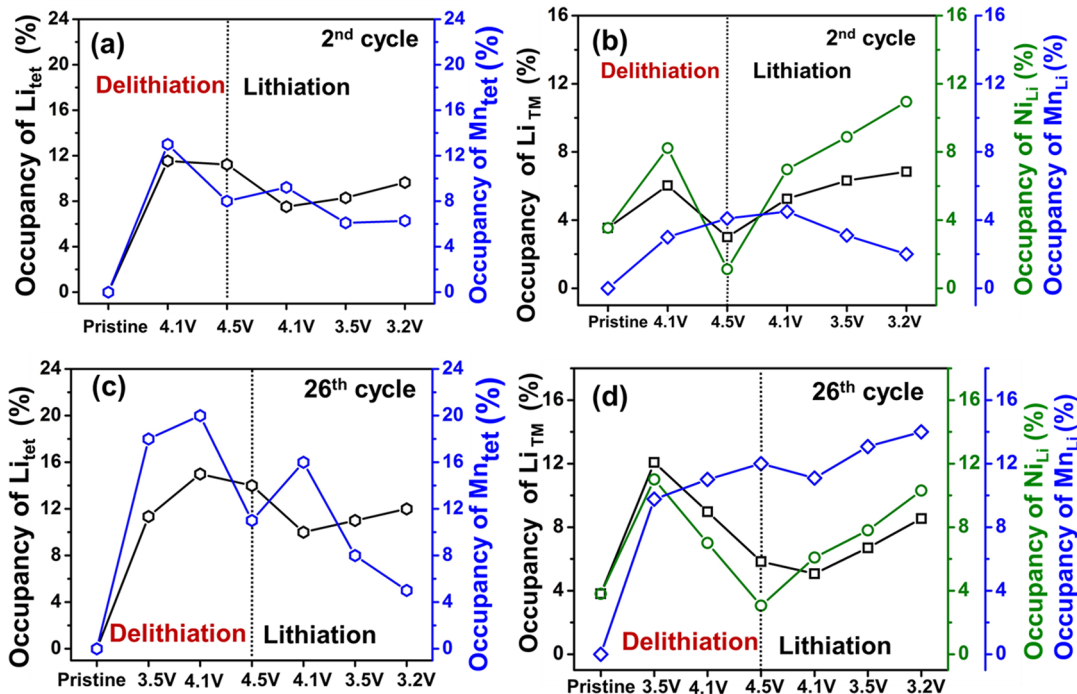


Figure 5. Percentage of Li_{tet} , Mn_{tet} , Li_{TM} , Ni_{Li} , and Mn_{Li} at different SOCs during the 2nd electrochemical cycle (a, b) and the 26th cycle (c, d).

spinel phase in the host layered HE5050 oxide after subsequent charge–discharge cycles likely alters the lithium (de)-intercalation process. It is important to note that the relocation of lithium ions in different crystallographic site(s) of the cycled HE5050 oxides might alter the site energy (possible Li–Li interaction), which will adversely affect the lithium (de)-intercalation chemistry and might ease lithium-ion movement during the lithium (de)intercalation process. Consequently, the average operating voltage of the cell could decrease, causing a depression of the voltage profile. In the following section we present an investigation of the cation migration paths and relocation sites of Li and metal ions for a LS transformation in the HE5050 oxide.

3.2. Cation Migration Pathways and Mechanism for LS Transformation. In an earlier article, Rana et al. indicated that the structural rearrangement in Li_2MnO_3 occurs due to repetitive shearing of oxygen layers and may not lead to spinel crystal structures in the oxide bulk.²⁰ They also mention that the structural changes in Li_2MnO_3 after extended cycling is very similar to that observed during the first cycle, during which a MnO_2 -type lattice is formed.²⁰ In that study, the authors also mention that a decrease in electrochemically active species may be a result of an inability of lithium ions to be reinserted to the transition-metal layers in the Li_2MnO_3 component. This eventually decreases cationic ordering in the structure, which is in agreement with the XRD and ND data presented in this article.

Trigonal layered ($\bar{R}\bar{3}m$ space group) and spinel (for example, spinel in $F\bar{d}\bar{3}m$ space group) unit cells are structurally correlated by group–subgroup schemes in the Bärnighausen formalism.²¹ Similar to the trigonal unit cell, a spinel unit cell is also O3 stacked and the LS structural transformation can occur via layer gliding and/or a direct movement of cations within the fixed oxygen anion (vacancy) arrays. The difference between the layered trigonal and the spinel (for example, if one considers LiMn_2O_4 spinel as model compound) structure is

that in the LiMn_2O_4 spinel, lithium atoms are present in the tetrahedral site and the TM(Mn) atoms are in the octahedral site of the lithium layer,²¹ whereas in the trigonal phase all the TM and Li ions are in the octahedral sites of their respective layers. The tetrahedral occupancy in the spinel structure increases the symmetry from $R\bar{3}m$ to $F\bar{d}\bar{3}m$ space group. Therefore, to track the LS transformation pathways in the cycled HE5050 oxide, the key is to investigate the cation occupancies at different cell voltages (Figure 1) and compare the crystallographic information on the 2nd and 26th cycles. We performed Rietveld refinement of the ND patterns of cycled HE5050 oxides, and the detailed steps for the refinement is presented below and the detailed crystallographic information, lattice parameter values, and the refined patterns are given in the Supporting Information. The refined cation occupancies at different SOCs in 2nd and 26th cycles including the pristine HE5050^{14a} oxide are plotted in Figure 5.

During Rietveld refinement, in the *first step*, the lattice parameters for both the trigonal and monoclinic phases were refined along with the phase percentages followed by refinement of the site occupancy factors (SOFs) of atoms in the trigonal phase (and/or otherwise mentioned). In the *second step*, SOFs for the Li and TM atoms were refined. The SOF of the lithium atoms in the lithium site (Li_{Li}) was refined freely. The occupancies of the Ni, Mn, and Co atoms in the TM site ($\text{Co/Mn/Ni}_{\text{TM}}$) were first refined with a constraint that the site was fully occupied. Once the occupancy of Li_{Li} was refined, a lithium atom was introduced in the octahedral 3a site of the TM layer (Li_{TM}) and the tetrahedral 6c site of the lithium layer (Li_{tet}) followed by the refinement of Li_{tet} and Li_{TM} occupancies. The occupancy of Li_{tet} and Li_{TM} was refined with a constraint that the total occupancy of the Li_{Li} , Li_{TM} , and Li_{tet} was equal to the occupancy of the Li_{Li} that was obtained in the *second step*. The presence of TM ions in the tetrahedral sites and in the octahedral 3b lithium site was also examined, and the change in agreement parameter values was monitored for improvements.

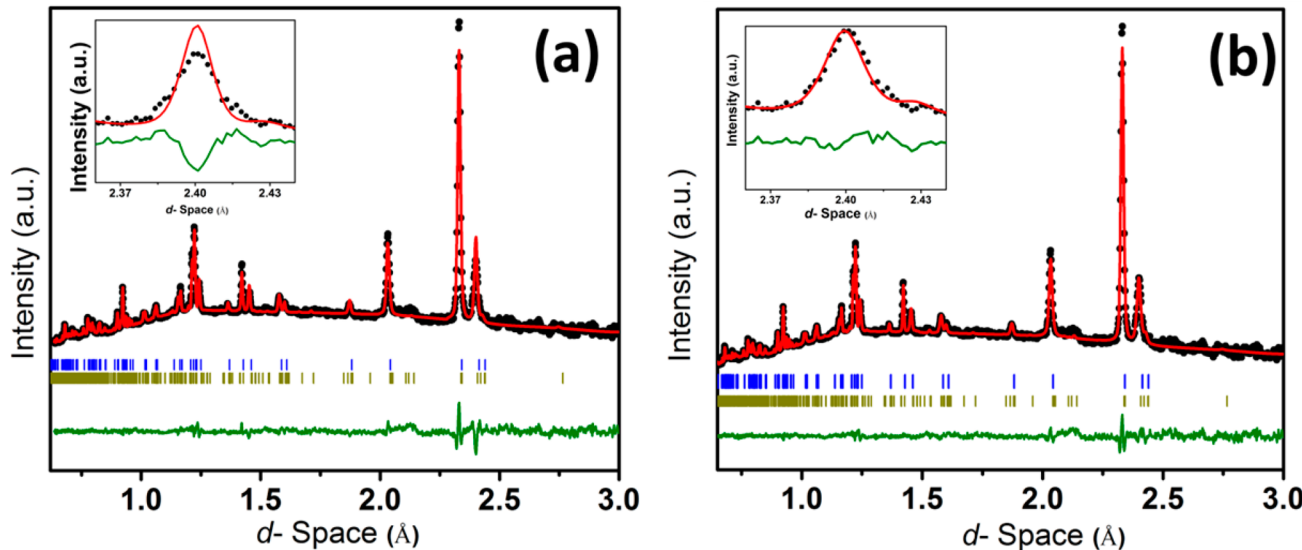


Figure 6. Refined ND patterns for HE5050 oxide collected at 4.1 V charged state without Li in the tetrahedral site of the lithium layer in the trigonal phase, model 2 (a), and with Li in the tetrahedral site of the lithium layer in the trigonal phase, model 3 (b).

The presence of TM atoms in the tetrahedral sites of the TM layer is unlikely because of electrostatic repulsion among the atoms present in the octahedral (3a) and tetrahedral sites of the TM layer. Therefore, the TM ions were allowed to reside in the tetrahedral site of the lithium layer (6c; 0, 0, x) only. Our refinements showed that placing Ni and Co in the tetrahedral site (Ni_{tet} , Co_{tet}) did not result in better agreement parameters; furthermore, including these occupancies yielded a negative SOF which indicated that there might be little or no Ni_{tet} and Co_{tet} in the cycled HE5050 oxide structures. However, Mn in the tetrahedral site of the lithium layer (Mn_{tet}) substantially improved the agreement parameter. In addition, introduction of TM ions in the lithium layer [i.e., Ni and Mn in the octahedral 3b site of the lithium layer (Ni_{Li} , Mn_{Li})] significantly improved the agreement parameters. Therefore, the Mn_{tet} , Mn_{Li} , and Mn_{TM} occupancies were refined with a constraint that the total occupancy of the Mn_{Li} , Mn_{TM} , and Mn_{tet} was equal to the occupancy of the Mn_{TM} obtained in the second step. The Ni_{Li} and Ni_{TM} were also refined with a constraint that the total occupancy of the Ni is equal to the occupancy of Ni obtained in the second step of the refinement.

The oxygen SOFs in trigonal and monoclinic phases were introduced and refined; oxygen vacancies in both phases significantly improved the agreement parameters. The composition of the cycled HE5050 oxide in the 2nd cycle (4.1 V charge and 3.2 V discharge) and 26th cycle (3.2 V charge and discharge) were calculated from the refined phase percentage and is reported, for clarity, in a one-component notation. The crystallographic information obtained from the Rietveld refinements for all the samples are given in the Supporting Information.

On the basis of the initial composition of the trigonal phase in the HE5050 oxide ($\text{LiCo}_{0.25}\text{Mn}_{0.375}\text{Ni}_{0.375}\text{O}_2$), 100% occupancy of Ni and Mn refers to an SOF of 0.375 and 100% occupancy of Co corresponds to a SOF of 0.25. The total lithium content in the cycled HE5050 oxide electrodes as a function of SOCs was calculated based on the capacity data (Table S1) and was compared with the results obtained from the refinement. The total lithium content at the beginning of the 2nd cycle was estimated to be 1.025 mol (assuming

irreversible capacity loss of 55 mA·h/g in the formation cycle, first cycle practical capacity as 314 mA·h/g) and 0.93 mol in the beginning of the 26th cycle (assuming 15% or 30 mA·h/g loss of capacity between the 2nd cycle and the 25th cycle).

3.2.1. During the 2nd Cycle. The structural refinement was initiated for the HE5050 oxide collected at the 4.1 V charge state during the 2nd cycle by a two-phase refinement of a trigonal unit cell where all the TM (Co, Mn, Ni) ions were in octahedral sites of the metal layer (3a), and the lithium ions were in the octahedral sites of the lithium layer (3b) (model 1). The agreement parameters with model 1 were found to be $R_{\text{WP}} = 2.30\%$, $R_p = 3.44$, and $\chi^2 = 3.67$. The presence of 6% lithium in the octahedral sites (3a) of the transition-metal layer (Li_{TM}) and 9% Ni in the octahedral sites (3a) of lithium layer (Ni_{Li}) resulted in $R_{\text{WP}} = 2.08\%$, $R_p = 3.18$, and $\chi^2 = 3.01$. During refinement, a Mn deficiency in the 3a site was observed, and the χ^2 value was further reduced by about 10% by placing 3% Mn in the octahedral sites (3b) of the lithium layer (Mn_{Li}). Therefore, with Li/Ni disorder and Mn_{Li} in the trigonal phase (model 2), a better fit was obtained, as compared to model 1 where Li/Ni disorder and Mn_{Li} were absent. The refined ND pattern with model 2 is shown in Figure 6a. Closer observation of the refined and experimental patterns revealed that, in some cases, the experimental peak intensity, for example, the (006) peak intensity, does not match the calculated intensity (see inset of Figure 6a). Substantial improvement in the peak fitting (for example, see the fitting of (006)) and further improvements in the agreement parameter value (χ^2 was reduced to 1.5) were obtained by model 3 (Figure 6b), in which 11% lithium atoms and 12% Mn atoms were placed in the tetrahedral 6c site of the lithium layer (0, 0, x ; $x = 0.125$).

Further, ND refinements showed 13% oxygen deficiency in overall composition that improved the agreement parameters ($R_{\text{WP}} = 1.78\%$, $R_p = 3.08$, $\chi^2 = 1.35$) (model 4); note that oxygen vacancies are expected in this oxide after the activation/formation cycle. The oxygen deficiency after initial cycle(s) is consistent with the report by Liu et al.²² Authors report the formation of oxygen vacancies and conclude that the activation barriers for transition-metal migration is significantly reduced by the presence of these vacancies. Although the current study

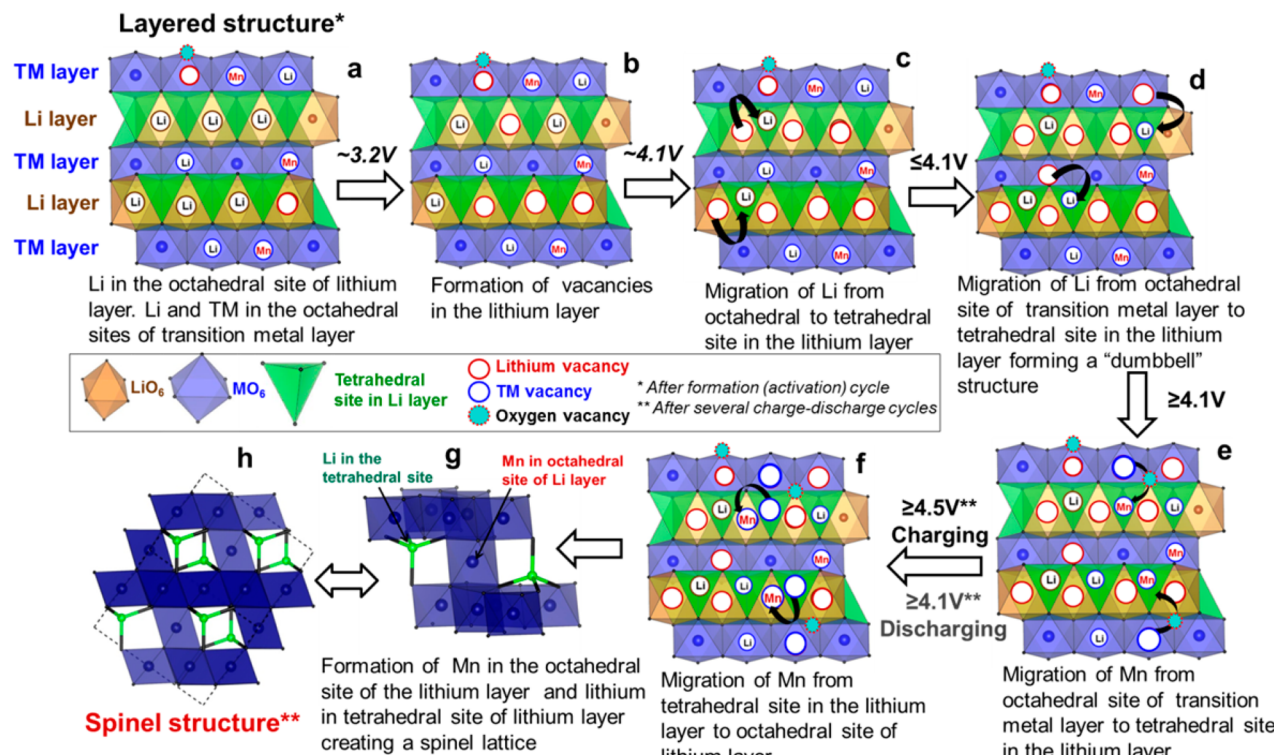


Figure 7. Proposed LS transformation mechanism in HES050 LMR composite oxide via formation of tetrahedral lithium in the lithium layer and migration of Mn from octahedral TM layer to octahedral site of lithium layer. Figures b–e correspond to the structural changes during charging. For details refer to section 3.2 in the text.

is unable to confirm whether the oxygen loss occurs only from the oxide surface or both from the surface and bulk, it clearly shows oxygen deficiency in the cycled HES050 oxides, which could assist in the cation migration described below.

From this point on, model 4 was considered as an initial model for refinement for the cycled HES050 oxides.

In the following section, we show how the SOFs of Li and TM ions vary during the charge and discharge processes as a function of cell voltage for the HE5050 oxides collected during the 2nd cycle (Figure 5). The Li_{tet} concentration is higher at 4.1 V than the pristine oxide. At 4.5 V, the percentage of Li_{tet} remained constant. In contrast, the occupancy of Mn_{tet} decreased in comparison to that of the 4.1 V charged state. The Mn_{Li} concentration increased, and the Ni_{Li} concentration decreased significantly. Interestingly, when the lithium ions and oxygen SOF in the monoclinic unit cell were <1, the agreement parameter was slightly improved. At the 4.1 V discharge state, the percentage of Li_{tet} decreased and Mn_{tet} slightly increased. The Ni_{Li} occupancy increased; however, the Mn_{Li} occupancy nearly remained constant. With further discharging, the Mn_{tet} slightly decreased at 3.5 V and remained constant at 3.2 V. In contrast, the occupancy of Li_{tet} increased on further discharging to 3.5 and 3.2 V. The Li_{TM} and Ni_{Li} occupancies increased during the discharge process regardless of the discharge voltage. These results yield a higher percentage of Ni_{Li} in the structure than the percentages of Mn_{Li} and Li_{TM} (see Figure 5b). In summary, at 3.2 V after completion of the 2nd cycle, the HE5050 oxide structure was more likely to contain a composite of trigonal and monoclinic phases with a significant amount of Mn and Li in the tetrahedral sites of lithium layer of trigonal phase. Therefore, the atomic distribution was not exactly like that of the pristine HE5050 oxide. The compound after the 2nd

cycle, the layered trigonal phase, can be written as $[(1-x-y-m)\text{Li}_y\text{Ni}_{\text{Li}}\square]_{3b}(x\text{Li}_{\text{tet}} z\text{Mn}_{\text{tet}})_{6c}\{m\text{Li}_{\text{TM}}(0.375-y)\text{Ni}(0.375-z)\text{Mn}0.25\text{Co}\}_{3a}\{\text{O}_{2-\delta}\}_{6c}$, where \square denotes the vacancies in the lithium layer (see Figure 7). The presence of Li_{tet} , Mn_{tet} in the lithium layer of layered trigonal phase after completion of the 2nd cycle might indicate a “defective/intermediate spinel” with formula $[\text{A}_{1-x}\text{B}_x]_{\text{tet}}[\text{A}_{x/2}\text{B}_{1-x/2}]_{\text{Oct}}\text{O}_4$, where A = Li and B = Mn. However, no “spinel peaks” were observed at a 3.2 V discharged state after completion of the 2nd cycle. Therefore, we speculate that the presence of Li_{tet} and Mn_{tet} in the lithium layer of the trigonal phase after the 2nd cycle might be the route to form a spinel-like framework over subsequent (26) cycles.

3.2.2. During the 26th Cycle. The change in cation occupancies in the cycled HE5050 oxides after 26 cycles to different SOCs were similar to the 2nd cycle; however, there are a few noteworthy distinctions to be made: (i) a higher percentage of Li_{tet} in the structure; (ii) the Mn_{tet} concentration increased during charging and decreased at 3.2 V discharged state; (iii) the concentration of Mn_{Li} increased during charging and did not decrease during discharging, suggesting an “irreversible” $\text{Mn}_{\text{TM}} \rightarrow \text{Mn}_{\text{Li}}$ migration; and (v) after discharging to 3.2 V, the phase percentage of LiMn_2O_4 spinel compound was calculated as 15%.

Therefore, the structure of HE5050 oxide after the 26th cycle is not structurally similar to the HE5050 oxide obtained after the 2nd cycle or the pristine HE5050 oxide. The structure of HE5050 oxide after the 26th cycle is a combination of trigonal, monoclinic, and spinel phases. From the current study, it is difficult to be certain whether there are many defects in a single phase (“splayered” phase) or three separate phases are present in the cycled (25 cycled) HE5050 oxide. The ND analysis also

provides evidence of irreversible Mn migration from the octahedral TM layer to the octahedral lithium layer and of the presence of excessive lithium in the tetrahedral site after 26 cycles, which could be the route for forming a spinel phase via the LS rearrangement mechanism (see below).

The finding that the percentage of LiMn_2O_4 is 15% after 26 cycles also indicates that major LS “restructuring” occurred during this period. Other spinel phases (for example, defective spinel where Mn is in the tetrahedral site) should not be ruled out; however, our ND refinement shows with the LiMn_2O_4 model (where lithium in the tetrahedral site and Mn in the octahedral site) better agreement parameters could be achieved.

To summarize, (1) Rietveld analysis shows cation rearrangement during initial cycles; however, irreversible and significant modification occupancies occur after extended cycling. (2) Rietveld analysis of the ND data showed an increase in lithium and Mn occupancies in the tetrahedral (0, 0, 0.125) sites during early charging and discharging (4.1 V), and the percentage increased over subsequent cycles. This finding provides evidence of the relocation of lithium atoms from Li_{oct} to Li_{tet} and accumulation over extended cycling. (3) The increase in Mn occupancies in the octahedral sites in the lithium layer indicates that migration of Mn_{TM} to Mn_{Li} might proceed via tetrahedral sites: $\text{Mn}_{\text{TM}} \rightarrow \text{Mn}_{(\text{Li})\text{tet}} \rightarrow \text{Mn}_{\text{Li}}$. This migration occurred during high-voltage charging (4.5 V) and low-voltage discharging (3.5 V). (4) The presence of lithium in the tetrahedral site and Mn in the octahedral site of lithium layer forms a spinel framework in oxides.

On the basis of the refined cation occupancies from the ND patterns presented above, the LS transformation pathways in cycled HE5050 oxide (cycled vs graphite) can be depicted as follows: (1) During the initial charging (after formation/activation cycles) (SOC \sim 3.2 V), lithium ions are extracted from the octahedral sites (3b) of the lithium layer (Li_{Li}), creating vacancies in the 3b sites (Figure 7a-b). When a sufficient amount of lithium vacancies are formed in the lithium layer (SOC \sim 4.1 V), the lithium ions (Li_{Li}) that are edge-shared with lithium octahedral sites in the TM metal layer may migrate to tetrahedral sites of the lithium layer, face-sharing with the lithium ion in the TM layer to form Li_{tet} (Figure 7c). This migration is inferred from the ND analysis where Li_{tet} substantially improves the agreement parameter at the 4.1 V charged state. (2) Subsequently, lithium ions in the octahedral transition-metal layer (Li_{TM}) may also migrate to tetrahedral sites in the lithium layer, which are shared on the opposite sides, forming an intermediate structure between layered and spinel phases, a “ $\text{Li}_{\text{tet}}-\odot-\text{Li}_{\text{tet}}$ dumbbell”,^{4,23} where \odot is the vacancy in the M layer) as proposed by a first-principle investigation (Figure 7d). The formation of $\text{Li}_{\text{tet}}-\odot-\text{Li}_{\text{tet}}$ dumbbell satisfies the thermodynamic requirement for migration of Mn to the lithium layer as proposed before.^{23a} (3) During charging at ≥ 4.1 V, the Mn in the octahedral site of transition metal (Mn_{TM}) ions may hop via oxygen vacancies to tetrahedral sites in the lithium layer to form Mn_{tet} (Figure 7e), as evident from the ND analysis (Figure 5c). (4) During subsequent charge/discharge cycles, these Mn_{tet} ions may migrate to “permanent” octahedral sites in the lithium layer to form Mn_{Li} (Figure 7f) during high-voltage charging (4.5 V) and low-voltage discharging (3.2 V).

These atomic rearrangements result in a substantially modified HE5050 structure where it now contains lithium in the tetrahedral sites (Li_{tet}) and Mn in the lithium layer (Mn_{Li}) (Figure 7g), which is the building block for a spinel/spinel-like

structure which was suggested by Gallagher et al. from their electrochemical cycling data.⁴ During repeated charge-discharge cycles, effects of the $\text{Mn}_{\text{TM}} \rightarrow \text{Mn}_{\text{Li}}$ migration become “permanent” and eventually growth of a spinel phase occurs (Figure 7h).

3.3. Plausible Routes To Overcome the LS Transformation Suppressing the Voltage Fade. Our results demonstrate the transformation in atomic occupancies and cation migration (i.e., Mn migration from the octahedral TM layer to the octahedral lithium layer and the lithium from octahedral to tetrahedral site of the lithium layer). The migration of Mn from octahedral sites of TM layer to tetrahedral sites of lithium layer is accessible only upon the availability of sufficient octahedral vacancies in the adjacent lithium layer (trivacancies).²⁴ The voltage fade in these high-voltage oxides is an intrinsic property and it is challenging to completely mitigate this adverse effect. However, the voltage fade can be minimized and the key to minimizing this LS transformation is to minimize the Mn and/or Li migration by techniques that include the following: (1) Partial doping with alkali atoms with higher ionic radii than Li, such as K and Na, that could act as fixed pillars in lithium layers. It is widely known that there are two types of sites (interstitial voids) in the cubic close-packed oxygen array, that is, one tetrahedral site and one octahedral site. In LiMn_2O_4 spinel structure, alkali Li occupies the tetrahedral 8a site and transition-metal Mn occupies the octahedral 16c site (which can be represented as $[\text{Li}]_{8a}[\text{Mn}]_{16c}\text{O}_4$). With a higher ionic radius than Li, K and Na cannot be accommodated in the tetrahedral sites within a fixed cubic-closed packed oxygen array and may not be favorable for layered to spinel conversion.²⁵ (2) Reducing the manganese content of LMR-NMC compounds would restrict the formation of Mn_{tet} , which is the major pathway to forming Mn_{Li} and may minimize the spinel phase formation.

4. CONCLUSIONS

The mechanism of layered to spinel structural evolution in HE5050 LMR-NMC oxides leading to voltage fade in a full-lithium-ion battery pouch cell (vs ConocoPhillips A12 natural graphite) was investigated. ND and XRD techniques were employed on harvested HE5050 oxides collected at different states of charge (SOCs) during the initial (2nd) and extended (26th) cycles, and important structural information was obtained. The results show the modification of a layered to spinel structure that occurs in a layered HE5050 LMR-NMC oxide after 26 cycles. Systematic neutron refinement on the oxides harvested in different SOCs suggests a specific cation migration path for this structural transformation. Analysis showed that the structural modification occurs due to migration of Mn from the octahedral TM layer to the octahedral lithium layer and dispersal of lithium from octahedral sites to tetrahedral sites in the lithium layer which became irreversible over the extended period of cycling to grow permanent spinel phase.

This mechanism of LS structure evolution may be applicable to all high-voltage LMR-NMC composite oxides of composition with high amounts of Mn, and the results provide important information on the methods to mitigate the structural evolution in high-voltage LMR-NMC cathodes for high-energy-density LIB applications.

■ ASSOCIATED CONTENT

§ Supporting Information

Neutron diffraction patterns and XRD analysis. This material is available free of charge via the Internet at <http://pubs.acs.org>.

■ AUTHOR INFORMATION

Corresponding Authors

*E-mail: mohantyd@ornl.gov.

*E-mail: wooddl@ornl.gov.

*E-mail: danielc@ornl.gov.

Author Contributions

C.D. and D.L.W. directed this research. D.M. led this work. D.M. fabricated the pouch cells, cycled the cells, analyzed/refined and interpreted the electrochemical and structural data, and wrote the manuscript. The electrochemical experiments were designed by D.P.A. A.H. and E.A.P. carried out the neutron powder diffraction experiment and were involved in structural refinement discussion. J.L. fabricated the HE5050 electrodes and helped in cycling the pouch cells.

Notes

The authors declare no competing financial interest.

■ ACKNOWLEDGMENTS

This research at Oak Ridge National Laboratory, managed by UT Battelle, LLC, for the U.S. Department of Energy (DOE), under contract DE-AC05-00OR22725, was sponsored by the Office of Energy Efficiency and Renewable Energy for the Vehicle Technologies Office's Applied Battery Research Program (Program Managers: Peter Faguy and David Howell). Part of this research was supported by the ORNL's User Facility at the Spallation Neutron Source, which is sponsored by the Scientific User Facilities Division, Office of Basic Energy Sciences. The HE5050 material was obtained from Argonne National Laboratory, in collaboration with Andrew Jansen and Bryant Polzin. The electrodes and cell fabrication, and pouch cell testing, were carried out at the DOE's Battery Manufacturing R&D Facility at Oak Ridge National Laboratory, which is supported by VTO's ABR Program. We thank Roberta A. Meisner at ORNL for her help in XRD data collection.

■ REFERENCES

- (1) (a) Howell, D. EV Everywhere Grand Challenge-Battery Obstacles and Opportunities. http://www1.eere.energy.gov/vehiclesandfuels/pdfs/ev_everywhere/5_howell_b.pdf. U.S. Department of Energy, 2012. (b) Danielson, D. T. U.S. Department of Energy-EV Everywhere grandchallenge blue print. http://www1.eere.energy.gov/vehiclesandfuels/electric_vehicles/pdfs/eveverywhere_blueprint.pdf, 2013. (c) Lee, J.; Urban, A.; Li, X.; Su, D.; Hautier, G.; Ceder, G. *Science* **2014**, *343*, 519.
- (2) (a) Thackeray, M. M.; Kang, S. H.; Johnson, C. S.; Vaughey, J. T.; Benedek, R.; Hackney, S. A. *J. Mater. Chem.* **2007**, *17*, 3112. (b) Johnson, C. S.; Li, N.; Lefief, C.; Vaughey, J. T.; Thackeray, M. M. *Chem. Mater.* **2008**, *20*, 6095.
- (3) Li, Y.; Bettge, M.; Polzin, B.; Zhu, Y.; Balasubramanian, M.; Abraham, D. P. *J. Electrochem. Soc.* **2013**, *160* (5), A3006.
- (4) Gallagher, K. G.; Croy, J. R.; Balasubramanian, M.; Bettge, M.; Abraham, D. P.; Burrell, A. K.; Thackeray, M. M. *Electrochim. Commun.* **2013**, *33*, 96.
- (5) Croy, J. R.; Gallagher, K. G.; Balasubramanian, M.; Chen, Z.; Ren, Y.; Kim, D.; Kang, S. H.; Dees, D. W.; Thackeray, M. M. *J. Phys. Chem. C* **2013**, *117* (13), 6525.
- (6) Bloom, I.; Trahey, L.; Abouimrane, A.; Belharouak, I.; Zhang, X.; Wu, Q.; Lu, W.; Abraham, D. P.; Bettge, M.; Elam, J. W.; Meng, X.; Burrell, A. K.; Banc, C.; Tenant, R.; Nanda, J.; Dudney, N. *J. Power Sources* **2014**, *249*, 509–524.
- (7) Mohanty, D.; Kalnaus, S.; Meisner, R. A.; Rhodes, K. J.; Li, J.; Payzant, E. A.; Wood, D. L., III; Daniel, C. *J. Power Sources* **2013**, *229*, 239–248.
- (8) Mohanty, D.; Sefat, A. S.; Li, J.; Meisner, R. A.; Rondinone, A. J.; Payzant, E. A.; Abraham, D. P.; Wood, D. L., III; Daniel, C. *Phys. Chem. Chem. Phys.* **2013**, *15* (44), 19496–19509.
- (9) Yang, X.; Wang, D.; Yu, R.; Bai, Y.; Shu, H.; Ge, L.; Guo, H.; Wei, Q.; Liu, L.; Wang, X. *J. Mater. Chem. A* **2014**, *2*, 3899–3911, doi: 10.1039/c3ta14513a.
- (10) (a) Zheng, J.; Gu, M.; Xiao, J.; Zuo, P.; Wang, C.; Zhang, J.-G. *Nano Lett.* **2013**, *13*, 3824–3830. (b) Boulineau, A.; Simonin, L.; Colin, J.-F.; Bourbon, C.; Patoux, S. *Nano Lett.* **2013**, *13*, 3857–3863, doi: 10.1021/nl401927s.
- (11) (a) Gu, M.; Belharouak, I.; Zheng, J.; Wu, H.; Xiao, J.; Genc, A.; Amine, K.; Thevuthasan, S.; Baer, D. R.; Zhang, J. G.; Browning, N. D.; Liu, J.; Wang, C. *ACS Nano* **2013**, *7*, 760–767. (b) Bettge, M.; Li, Y.; Gallagher, K.; Zhu, Ye.; Wu, Q.; Lu, W.; Bloom, I.; Abraham, D. P. *J. Electrochem. Soc.* **2014**, *160* (11), A2046–A2055.
- (12) Pol, V. G.; Li, Y.; Dogan, F.; Secor, E.; Thackeray, M. M.; Abraham, D. P. *J. Power Sources* **2014**, *258*, 46.
- (13) Mohanty, D.; Sefat, A. S.; Li, J.; Meisner, R. A.; Rondinone, A. J.; Payzant, E. A.; Abraham, D. P.; Wood, D. L., III; Daniel, C. *Phys. Chem. Chem. Phys.* **2013**, *15*, 19496.
- (14) (a) Mohanty, D.; Huq, A.; Payzant, E. A.; Sefat, A. S.; Li, J.; Abraham, D. P.; Wood, D. L., I; Daniel, C. *Chem. Mater.* **2013**, *25*, 4064–4070. (b) Whitfield, P. S.; Davidson, I. J.; Cranswick, L. M. D.; Swainson, I. P.; Stephens, P. W. *Solid State Ionics* **2005**, *176*, 463.
- (15) Oak Ridge National Laboratory, Battery Manufacturing facility, <http://web.ornl.gov/sci/ees/transportation/bmf.shtml>.
- (16) Huq, A.; Hodges, J. P.; Gourdon, O.; Heroux, L. Z. *Kristallogr.* **2011**, *1*, 127–135.
- (17) Toby, B. H. *J. Appl. Crystallogr.* **2001**, *34*, 210.
- (18) Larsen, A. C.; Von Dreele, R. B. General Structure Analysis System (GSAS). *Los Alamos National Laboratory Report LAUR 86-748*; Los Alamos National Laboratory: Los Alamos, NM, 2004.
- (19) Lee, E. S.; Huq, A.; Chang, H.-Y.; Manthiram, A. *Chem. Mater.* **2012**, *24*, 600–612.
- (20) Rana, J.; Stan, M.; Kloepsch, R.; Li, J.; Schumacher, G.; Welter, E.; Zizak, I.; Banhart, J.; Winter, M. *Adv. Energy Mater.* **2014**, *4*, 1300998, doi: 10.1002/aenm.201300998.
- (21) Yahia, H. B.; Shikano, M.; Kobayashi, H. *Chem. Mater.* **2013**, *25*, 3687–3701, doi: 10.1021/cm401942t.
- (22) Liu, H.; Fell, C. R.; An, K.; Cai, L.; Meng, Y. S. *J. Power Sources* **2014**, *240*, 772.
- (23) (a) Xu, B.; Fell, C. R.; Chi, M.; Meng, Y. S. *Energy Environ. Sci.* **2011**, *4*, 2223. (b) Armstrong, A. R.; Dupre, N.; Paterson, A. J.; Grey, C. P.; Bruce, P. G. *Chem. Mater.* **2004**, *16*, 3106. (c) Kim, S.; Ma, X.; Ong, S. P.; Ceder, G. *Phys. Chem. Chem. Phys.* **2012**, *14*, 15571–15578.
- (24) Van der Ven, A.; Ceder, G.; Asta, M.; Tepesch, P. D. *Phys. Rev. B* **2001**, *64*, 184307.
- (25) Li, Q.; Li, G.; Fu, C.; Luo, D.; Fan, J.; Li, L. *ACS Appl. Mater. Interfaces* **2014**, *6* (13), 10330.